Electrochemical Materials and Technologies

ARTICLE

Electrochemical Materials and Technologies

eISSN: 2949-0561

Cite this: Electrochem. Mater. Technol. 4 (2025) 20254053

Details on oxygen surface exchange mechanism over $Pr_{1.6}Ca_{0.4}Ni_{1-y}Cu_yO_{4+\delta}$ solid oxide fuel cell/electrolyzer air electrodes

Vladislav Sadykov [a], Ekaterina Sadovskaya [a], Nikita Eremeev [a] *, Elena Pikalova [b]

Received: 8 June 2025
Accepted: 16 June 2025
Published online: 20 June 2025

DOI: 10.15826/elmattech.2025.4.053

In the design of solid oxide fuel cell/electrolyzer air electrodes, the oxygen mobility and surface reactivity are of paramount importance. In this study, the oxygen surface heteroexchange rate is examined for a series of promising electrode materials, $Pr_{1.6}Ca_{0.4}Ni_{1-y}Cu_yO_{4+\delta}$ (y = 0.0–0.4). The investigation encompasses the relationship between this rate and the structural, surface, and electrochemical properties. Single-phase materials synthesized by a nitrate combustion technique using glycerol as a fuel possess an orthorhombic structure. The oxygen surface reactivity is studied by the temperature-programmed isotope exchange of oxygen with $^{18}O_2$ in a flow reactor. The values of the oxygen heteroexchange rate (R^*) and surface exchange constant (k^*) are acquired using mathematical modeling. The isotope exchange between the gas oxygen and the sample surface occurs primarily via the R^2-type of exchange mechanism, i.e., the simultaneous exchange of two atoms of the oxygen molecule with two atoms of oxygen in the sample surface. The process is limited by surface exchange of oxygen characterized by high values of surface exchange constant (up to ~ 10^{-5} cm/s at 700 °C). The best characteristics are achieved for the $Pr_{1.6}Ca_{0.4}Ni_{1-y}Cu_yO_{4+\delta}$ samples, y = 0.0–0.2. There is a correlation of the oxygen exchange kinetic parameters (surface exchange constant, tracer diffusion coefficient) with the electrochemical properties of the electrodes according to the Adler–Lane–Steele model.

keywords: solid oxide fuel cells, solid oxide electrolyzers, layered nickelates, oxygen surface exchange, isotope exchange of oxygen

1. Introduction

First-order Ruddlesden–Popper (RP) phases $Ln_2MO_{4+\delta}$ (Ln = La, Pr, Nd, etc.; M = Co, Ni, Cu, etc.) have attracted considerable attention due to their efficient application in solid oxide fuel cells (SOFCs) and electrolyzers (SOEs) as air [1–7] and fuel [2, 5, 8–10] electrodes, oxygen separation membranes [11–13], and components of catalysts for hydrogen and syngas production [11, 14]. They have also demonstrated promise in a variety of other applications [15, 16]. Their high performances in such applications are provided by the distinguishable features of these materials due to a layered structure comprising alternating perovskite and rock-salt layers. Among their advances are high mixed ionic-electronic conductivity, oxygen mobility and surface reactivity, moderate thermal expansion coefficients and chemical stability under operating conditions (except for $Pr_2NiO_{4+\delta}$). In particular, achieving a high level of oxygen mobility and surface reactivity is imperative to ensure the effective operation of the SOFC/SOE air electrodes. In this case, the electrode reaction (oxygen reduction/evolution reactions, ORR/OER) is not limited by a triple-phase boundary (gas – electrode – electrolyte), but occurs on a double-phase boundary (gas–electrode) as well [3–5, 7, 17–19]. There has been an Adler–Lane–Steele (ALS) model, in which the mixed ion-electron conducting (MIEC) electrode performance correlates with the oxygen self-diffusion coefficient and surface exchange constant values of the electrode material as well as the microstructure features [19–21].

Excellent oxygen transport properties of first-order RP phases, including Ln nickelates, are attributed to a cooperative mechanism of oxygen migration involving both regular and highly mobile interstitial oxygen

a: Federal Research Center Boreskov Institute of Catalysis SB RAS, Novosibirsk 630090, Russia
b: Institute of High-Temperature Electrochemistry UB RAS, Ekaterinburg 620066, Russia

* Corresponding author: yeremeev2l@catalysis.ru

presented in a high excess [3, 7, 12, 19, 22–27]. This mechanism (known also as an interstitial mechanism) involves the movement of interstitial oxygen in a rock salt layer across the Ln_3 triangle into the apical position of NiO_6 octahedra in a perovskite layer, and this apical oxygen is displaced across the neighboring Ln_3 triangle into the interstitial position. Such a mechanism provides high values of the oxygen self-diffusion coefficient (up to ~ 10^{-8}–10^{-7} cm²/s at 700 °C). The doping of *A*- and *B*-sites with various cations has been demonstrated to exert a substantial influence on the cooperative mechanism and, consequently, on the oxygen mobility of the RP phases [22, 24–30]. This is related to the interstitial oxygen content, the size of the dopant cation, as well as other structural and defect features.

Another salient feature pertains to oxygen surface reactivity, given that surface exchange of oxygen in the oxide and in the gas phase constitutes a pivotal process in ORR/OER [31–33]. Interstitial oxygen in the rock salt layers and regular oxygen in the perovskite layers have been demonstrated to be two major active centers for ORR and OER. The governing factors have been demonstrated to be oxygen adsorption and incorporation. *Ln* nickelates have been shown to exhibit high values of the oxygen surface exchange constant (up to ~ 10^{-7}–10^{-6} cm/s at 700 °C) [26, 28, 29, 32, 34–36]. The surface exchange of oxygen for RP phases typically occurs via R^1 and R^2 type of exchange mechanisms according to the Muzykantov's classification [37, 38], i.e., the simultaneous exchange of one or two oxygen atoms from the oxygen molecule with one or two oxygen atoms from the oxide surface, respectively. The rate-determining steps in this process are believed to be either oxygen dissociative adsorption and incorporation, or both stages may be competing depending on the sample composition and synthesis technique. It has been demonstrated that interstitial oxygen plays an important role in the incorporation of adsorbed oxygen [26, 32, 33, 35]. The oxygen surface exchange process is influenced by the dopant nature and content due to the effects of surface properties, defects, the rate-determining step, the affinity of oxygen to *A*- and *B*-site cations, and the surface diffusion energy barrier [27–29, 33–36].

In several recent works performed jointly in IHTE UB RAS, UrFU and BIC SB RAS [39–41], the physicochemical properties of $Pr_{1.6}Ca_{0.4}Ni_{1-y}Cu_yO_{4+\delta}$ (y = 0.0–0.4) materials perspective for air electrodes in various electrochemical devices have been studied. The materials have demonstrated a moderate level of the total conductivity (σ_{tot}, 155–90 S/cm at 700 °C depending on the Cu content) and the thermal expansion coefficient (TEC, 13.5–13.7 × 10^{-6} K^{-1} in the range of 100–900 °C). They exhibit excellent phase stability and chemical and thermomechanical compatibility with CeO_2- and $BaCe(Zr)O_3$-based electrolytes. Moreover, Cu-doping was found to enhance the electrochemical activity of the related electrodes. For instance, the polarization resistance of the $Pr_{1.6}Ca_{0.4}Ni_{0.8}Cu_{0.2}O_{4+\delta}$ electrode is in the range of 0.19–0.27 Ω · cm² (at 700 °C) depending on the electrolyte substrate [39]. According to the data obtained using temperature-programmed isotope exchange of oxygen (TPIE) with $C^{18}O_2$ in a flow reactor, the highest D^* value for O_{fast}, moving via the cooperative mechanism, was demonstrated for $Pr_{1.6}Ca_{0.4}Ni_{0.8}Cu_{0.2}O_{4+\delta}$ equal to 9.4 · 10^{-8} cm²/s at 700 °C [41]. To complement these findings, in the present work, the surface exchange properties of these materials have been studied by TPIE with $^{18}O_2$. The correlation of the electrode performance with oxygen surface heteroexchange rate and diffusion coefficient values according to the ALS model has been demonstrated.

2. Experimental

The materials of the $Pr_{1.6}Ca_{0.4}Ni_{1-y}Cu_yO_{4+\delta}$ (y = 0.0–0.4, PCNO, PCNCO01–PCNCO04) series were synthesized by nitrate combustion using glycerol as a fuel, as described in detail in the works [39, 41].

The structural properties of the materials were examined after the final step by powder X-ray diffraction (XRD) analysis using a Shimadzu XRD-7000 diffractometer (Japan) with a graphite monochromator with Cu $K\alpha_1$ radiation at room temperature in air. The XRD patterns were obtained over the angle range of $10 < 2\theta < 90$ with a step size of 0.02 ° and an exposure time of 5 s at each point.

A Brunauer–Emmett–Teller (BET) method was employed to determine the specific surface area values, utilizing a SORBI N.4.1 analyzer (Meta, Russia).

The oxygen surface reactivity of the samples was studied by the temperature-programmed isotope exchange (TPIE) of oxygen with $^{18}O_2$ in a flow reactor. The samples (0.25–0.5 mm fraction, 50 mg weight) were loaded into a quartz tubular reactor (inner diameter of 3 mm). Pretreatment was carried out at 700 °C during 0.5 h in a flow of 1 % O_2 + He (flow rate of 25 ml/min) followed by cooling. The TPIE experiments were carried out in 1 % $^{18}O_2$ + He (flow rate of 25 ml/min) while heating from 50 °C to 800 °C with a ramp of 5 °C/min. The gas phase composition at the reactor outlet was analyzed by a UGA 200 mass spectrometer (Stanford Research Systems, USA). The dependencies of the ^{18}O atomic fraction (α) and the $^{16}O^{18}O$ molecular fraction (f_{34}) in the gas phase were used for calculations of isotope

exchange kinetic parameters via mathematical modeling [29, 42, 43].

3. Theory

3.1. Dissociative adsorption-desorption and three types of exchange mechanisms

The surface exchange of oxygen in the molecular oxygen – solid oxide systems is known to occur via the Muzykantov–Boreskov mechanism, or the dissociative adsorption-desorption mechanism [26, 29, 35, 36, 44–46], which includes the steps of:

• physical adsorption;

• chemisorption of an oxygen molecule with its dissociation (Equations 1–3):

$$O_{2\,(g)} + 2(\quad)_a = 2(O)_a, \tag{1}$$

$$O_{2\,(g)} + (\quad)_a + [\quad]_S = (O)_a + [O]_S, \tag{2}$$

$$O_{2\,(g)} + 2[\quad]_S = 2[O]_S, \tag{3}$$

where $(\quad)_a$ and $[\quad]_S$ are the adsorption site and oxygen vacancy on the surface, respectively, $(O)_a$ and $[O]_S$ are the adsorbed (weakly bound, capable of surface diffusion) and surface (strongly bound with oxygen vacancy) oxygen species, respectively;

• incorporation (Equation 4):

$$(O)_a + [\quad]_S = (\quad)_a + [O]_S. \tag{4}$$

For isotope exchange with $^{18}O_2$ (as well as other molecules containing two identical atoms), according to the Muzykantov's classification [37, 38], there are three types of exchange mechanism:

• Homoexchange

• R^0-type (0-atomic type, I type, Equation 5):

$$^{18}O_2 + {}^{16}O_2 = 2\,{}^{16}O^{18}O; \tag{5}$$

• Heteroexchange

• R^1-type (1-atomic type, II type, Equations 6 and 7):

$$^{18}O_2 + [^{16}O] = {}^{16}O^{18}O + [^{18}O], \tag{6}$$

$$^{16}O^{18}O + [^{16}O] = {}^{16}O_2 + [^{18}O]; \tag{7}$$

• R^2-type (2-atomic type, III type, Equations 8–10):

$$^{18}O_2 + 2[^{16}O] = {}^{16}O_2 + 2[^{18}O], \tag{8}$$

$$^{18}O_2 + [^{16}O] + [^{18}O] = {}^{16}O^{18}O + 2[^{18}O], \tag{9}$$

$$^{16}O^{18}O + 2[^{16}O] = {}^{16}O_2 + [^{16}O] + [^{18}O]. \tag{10}$$

3.2. Mathematical models for description of TPIE $^{18}O_2$ data

There are two models applied in this work for the description of isotope exchange data:

• Model 1 (Equations 11–17) considering a direct exchange of molecular oxygen with the oxygen of the oxide surface [29];

• Model 2 (two-step model, Equations 18–25) considering the exchange of the molecular oxygen with the chemisorbed oxygen atoms ($O_2^{GAS} \leftrightarrow O_{ADS}$, as formed according to the Equations 1–3) followed by the exchange of the chemisorbed oxygen atoms with the surface oxygen of the oxide surface ($O_{ADS} \leftrightarrow O_S$, Equation 4).

Model 1

$$\frac{\partial \alpha_G}{\partial t} + \frac{1}{\tau}\frac{\partial \alpha_G}{\partial \xi} = \frac{N_S}{N_G} R(\alpha_S - \alpha_G) \tag{11}$$

$$\frac{\partial \alpha_S}{\partial t} = R(\alpha_G - \alpha_S) - \frac{N_{BULK}}{N_S}\frac{D}{h^2}\frac{\partial \alpha_{BULK}}{\partial \eta}\bigg|_{\eta=0} \tag{12}$$

$$\frac{\partial \alpha_{BULK}}{\partial t} = \frac{D}{h^2}\frac{\partial^2 \alpha_{BULK}}{\partial \eta^2} \tag{13}$$

In the case of R^0-type of exchange mechanism:

$$\frac{\partial f_{34}}{\partial t} + \frac{1}{\tau}\frac{\partial f_{34}}{\partial \xi} = \frac{N_S}{N_G} R^0(2\alpha_G(1-\alpha_G) - f_{34}) \tag{14}$$

In the case of R^1-type of exchange mechanism:

$$\frac{\partial f_{34}}{\partial t} + \frac{1}{\tau}\frac{\partial f_{34}}{\partial \xi} = \frac{N_S}{N_G}(R^1(\alpha_G(1-\alpha_S) + 2\alpha_S(1-\alpha_G) - f_{34}), R^1 = 2R \tag{15}$$

In the case of R^2-type of exchange mechanism:

$$\frac{\partial f_{34}}{\partial t} + \frac{1}{\tau}\frac{\partial f_{34}}{\partial \xi} = \frac{N_S}{N_G}(R^2(2\alpha_S(1-\alpha_S) - f_{34}), R^2 = R \tag{16}$$

Initial and boundary conditions:

$$t = 0: \alpha = \alpha_{OX} = f_{34} = 0$$
$$\xi = 0: \alpha = \alpha^{input}, f_{34} = f_{34}^{input} \tag{17}$$

Here, N_G, N_S and N_{BULK} are the numbers of atoms in the gas phase, on the surface and in the bulk of the oxide, respectively; R^1 and R^2 are the exchange rates via R^1- and

R^2-types of mechanism, respectively, D is the tracer diffusion coefficient, h is the characteristic size of the oxide particle; η is a dimensionless distance from the oxide surface; α_G, α_{OX}, α_S and α_{BULK} are ^{18}O fractions in the gas phase, in the oxide, on the surface and in the bulk of the oxide, respectively; t is time; τ is the contact time; ξ is dimensionless length of the sample layer in the reactor.

Model 2

$$\frac{\partial \alpha_G}{\partial t} + \frac{1}{\tau}\frac{\partial \alpha_G}{\partial \xi} = \frac{N_{ADS}}{N_G} R(\alpha_{ADS} - \alpha_G) \quad (18)$$

$$\frac{\partial \alpha_{ADS}}{\partial t} = R(\alpha_G - \alpha_{ADS}) - \frac{N_S}{N_{ADS}}(\alpha_S - \alpha_{ADS}) \quad (19)$$

$$\frac{\partial \alpha_S}{\partial t} = R(\alpha_{ADS} - \alpha_S) - \frac{N_{BULK}}{N_S}\frac{D}{h^2}\frac{\partial \alpha_{BULK}}{\partial \eta}\Big|_{\eta=0} \quad (20)$$

$$\frac{\partial \alpha_{BULK}}{\partial t} = \frac{D}{h^2}\frac{\partial^2 \alpha_{BULK}}{\partial \eta^2} \quad (21)$$

In the case of R^0-type of exchange mechanism:

$$\frac{\partial f_{34}}{\partial t} + \frac{1}{\tau}\frac{\partial f_{34}}{\partial \xi} = \frac{N_{ADS}}{N_G} R^0(2\alpha_G(1-\alpha_G) - f_{34}) \quad (22)$$

In the case of R^1-type of exchange mechanism:

$$\frac{\partial f_{34}}{\partial t} + \frac{1}{\tau}\frac{\partial f_{34}}{\partial \xi} = \frac{N_{ADS}}{N_G}(R^1(\alpha_G(1-\alpha_{ADS}) + \alpha_{ADS}(1-\alpha_G) - f_{34}), R^1 = 2R \quad (23)$$

In the case of R^2-type of exchange mechanism:

$$\frac{\partial f_{34}}{\partial t} + \frac{1}{\tau}\frac{\partial f_{34}}{\partial \xi} = \frac{N_{ADS}}{N_G} R^2(2\alpha_{ADS}(1-\alpha_{ADS}) - f_{34}), \quad R^2 = R \quad (24)$$

Initial and boundary conditions:

$$t = 0: \alpha_G = \alpha_{ADS} = \alpha_S = \alpha_{BULK} = f_{34} = 0$$
$$\xi = 0: \alpha_G = \alpha^{input}, f_{34} = f_{34}^{input} \quad (25)$$

Here, α_{ADS} is ^{18}O fraction of the adsorbed oxygen, N_{ADS} is the number of adsorbed oxygen atoms.

3.3. Adler–Lane–Steele model

For elucidation of the correlations of the electrochemical performance of electrodes with the oxygen exchange and diffusion rates, the ALS model (Equation 26) is applied [20, 21, 28, 47]:

$$R_p = \frac{RT}{4F}\sqrt{\frac{\pi_{tort}}{(1-\pi_{por})4S_{sp}C_O D^*_{over}k^*}}, \quad (26)$$

where R_p is the polarization resistance of the electrode; F is the Faraday constant; π_{tort} and π_{por} are the electrode tortuosity and porosity, respectively; S_{sp} is the specific surface area of the electrode; C_O is the molar concentration of oxide anions in the oxide; D^*_{over} is the mean integral oxygen tracer diffusion coefficient; k^* is the oxygen surface exchange constant.

Hence, the correlations between R_p and $(D^*_{over}k^*)^{0.5}$ can be considered. D^*_{over} can be calculated considering the diffusion coefficients of various oxygen forms. k^* can be calculated as being proportional to the oxygen surface heteroexchange rate [35, 48].

4. Results and discussion

4.1. Structural features and oxygen content

According to the XRD data (Figure 1), all $Pr_{1.6}Ca_{0.4}Ni_{1-y}Cu_yO_{4+\delta}$ (y = 0.0–0.4) samples are single-phase and possess an orthorhombic structure with the *Bmab* space group. The refinement of unit cell parameters was carried out using the Rietveld full-profile analysis method with the FullProf Suite software (presented in Table 1). The unit cell parameter c increases with increasing Cu content in the series, whereas the a and b parameters decrease, which can be related to the tendency of Jahn–Teller Cu^{2+} ions to form elongated CuO_6 octahedra [49, 50]. These multidirectional changes result in an increase in the unit cell volume. More detailed data on the structural characterization of samples are presented in the authors' previous works [39, 41].

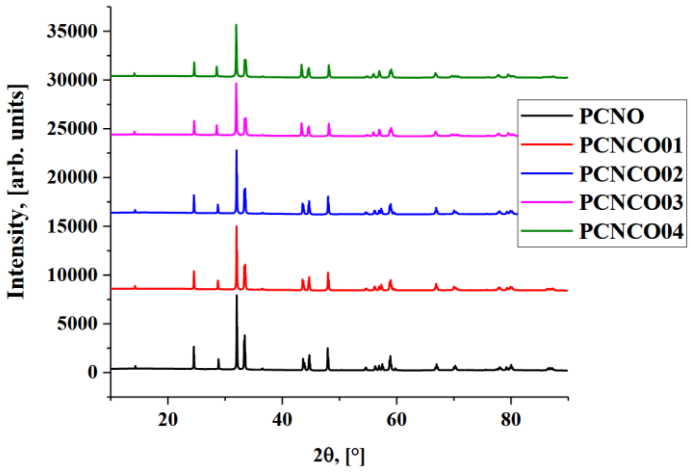

Figure 1 XRD patterns obtained at room temperature for the as-synthesized $Pr_{1.6}Ca_{0.4}Ni_{1-y}Cu_yO_{4+\delta}$ materials. Reproduced from Ref. [41] under the CC BY 4.0 license.

Table 1 – Structure parameters and oxygen content for the $Pr_{1.6}Ca_{0.4}Ni_{1-y}Cu_yO_{4+\delta}$ series [39, 41].

y	0.0	0.1	0.2	0.3	0.4
Sample designation	PCNO	PCNCO01	PCNCO02	PCNCO03	PCNCO04
a, [Å]	5.3537(1)	5.3441(2)	5.3340(3)	5.3270(1)	5.3220(2)
b, [Å]	5.3726(2)	5.3686(3)	5.3626(3)	5.3580(1)	5.3560(2)
c, [Å]	12.3706(3)	12.4166(3)	12.4659(3)	12.5051(4)	12.5521(4)
V, [Å^3]	355.82(2)	356.24(1)	356.58(1)	356.98(2)	357.8(2)
4+δ	4.12	4.09	4.02	3.97	4.00

The oxygen content according to the TGA data [39, 41] is given in Table 1. The examples of temperature dependencies of oxygen overstoichiometry according to the TGA data in air are given in Figure 2. The overall oxygen content decreases with increasing temperature due to the oxygen desorption, which is typical for first-order RP phases. More detailed data on the oxygen content of the samples are presented in the authors' previous works [39, 41].

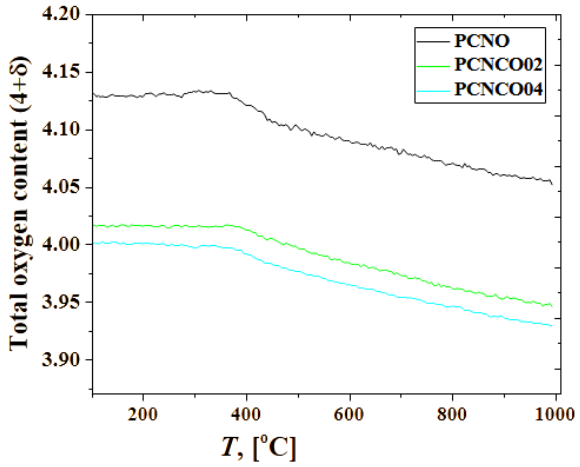

Figure 2 Total oxygen content in the materials of the $Pr_{1.6}Ca_{0.4}Ni_{1-y}Cu_yO_{4+\delta}$ series, as defined via TGA data in air. Reproduced from Ref. [41] under the CC BY 4.0 license.

4.2. Oxygen surface reactivity

Figure 3 (upper image) demonstrates the dependencies for the ^{18}O atomic fractions in the gas phase oxygen (α_G) acquired for the $Pr_{1.6}Ca_{0.4}Ni_{1-y}Cu_yO_{4+\delta}$ samples during TPIE run. The variation of α_G depends on both surface exchange rates and bulk diffusion of oxygen. The higher the total rate of O_2 exchange with the oxide oxygen – the lower the temperature at which a significant decrease in α_G is observed. As illustrated in Figure 3, the $\alpha_G(T)$ dependencies for the PCNO and PCNCO01 samples are highly analogous. A slight decrease in the observed exchange rate for the PCNCO01 sample is most likely related to the higher specific surface area (S_{sp} is 1.5 m^2/g and 2.1 m^2/g for the PCNO and PCNCO01 samples, respectively). The oxygen surface exchange rate demonstrates a substantial decline when the Cu content is

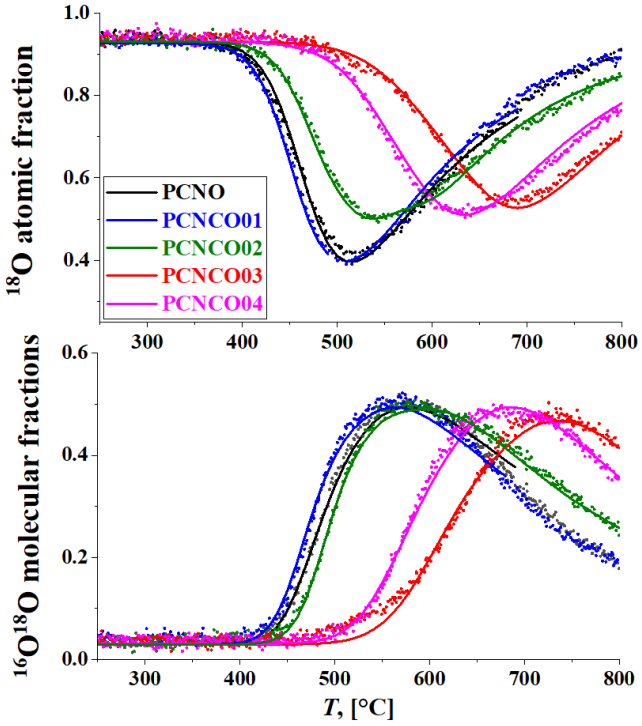

Figure 3 Temperature-programmed isotope exchange of oxygen with $^{18}O_2$ in the flow reactor for the $Pr_{1.6}Ca_{0.4}Ni_{1-y}Cu_yO_{4+\delta}$ samples. Points – experiment, lines – modeling.

elevated from $y = 0.1$ to 0.3 (PCNCO01–03). However, a subsequent increase in the Cu content to $y = 0.4$ (PNCNO04) results in an increase in the oxygen surface exchange rate.

The potential causes of the decrease in the oxygen surface exchange rate with increasing the Cu content in the $Pr_{1.6}Ca_{0.4}Ni_{1-y}Cu_yO_{4+\delta}$ ($y = 0.0$–0.3) are evident. It has been established that CuO exhibits an oxygen surface heteroexchange rate with $^{18}O_2$ that is approximately one order of magnitude lower than that of NiO [51]. $Pr_2CuO_{4+\delta}$ exhibits reduced activity in the isotope exchange of oxygen in comparison with $Pr_2NiO_{4+\delta}$ [52].

However, Miyoshi et al. [53] have shown that the substitution of Ni with Cu has a significant impact on both mixed conductivity and oxygen diffusion. Specifically, two compositions of $Pr_2Ni_{0.8}Cu_{0.2}O_{4+\delta}$ and $Pr_2Ni_{0.75}Cu_{0.25}O_{4+\delta}$ showed considerably higher oxygen permeation rates of 60 and 100 μmol · min^{-1} · cm^{-2} at

1000 °C through a membrane with a thickness of 0.5 mm than that of the other *B*-site doped (with Co, Fe, Mn, Zn, Al, Ga, Mg) $Pr_2NiO_{4+\delta}$ oxides.

Yashima et al. [54], using Density Functional Theory calculations, have shown that in the $Pr_2Ni_{1-x}Cu_xO_{4+\delta}$ crystal structure the degeneracy in molecular or ionic complexes with electronically degenerate states can be removed by a distortion where the Cu–O bond length in the direction perpendicular to the perovskite layer (bonds between Cu^{2+} and apical oxygen ions), increases. Due to the distortion, the bonds between Cu^{2+} and the apical oxygen ions are weaker than the bonds between Cu^{2+} and the equatorial oxygen ions. Thereby, the apical ion can contribute to oxygen ion diffusion by moving into the interstitial site. This creates a vacancy at the apical site while simultaneously increasing the number of ionic charge carriers.

It is established that highly mobile interstitial oxygen plays a crucial role in the surface exchange for RP phases [26, 32, 33, 35]. The observed decrease in the oxygen surface exchange rate in the row of $Pr_{1.6}Ca_{0.4}Ni_{1-y}Cu_yO_{4+\delta}$ (y = 0.0–0.3) (Figure 3) is in agreement with the decrease in the interstitial oxygen content (Table 1), as well as the decrease in the oxygen tracer diffusion coefficient values with increasing Cu content, as previously demonstrated by $C^{18}O_2$ TPIE [41].

The PCNCO04 sample exhibits slightly higher oxygen content (δ = 0.00) compared to PCNCO03 (δ = –0.03, Table 1) [39, 41].

A higher surface reactivity for the PCNCO04 sample compared to the PCNCO03 one may also be related to the surface properties. As demonstrated in the work [39] by X-ray photoelectron spectroscopy (XPS), there are four forms of surface oxygen for the PCNCO samples with a binding energy of 528.8, 530.15, 531.2 and 532.6 eV (Table 2). The first two forms likely correspond to the structural oxygen associated with Ni and Pr [39]. The third form may correspond to the oxygen within $(CO_3)^{2-}$ groups, as well as adsorbed oxygen and oxygen in the defect sites of the crystal lattice [39, 55, 56]. The peak at 532.6 eV may be associated with adsorbed water [39, 54]. The PCNCO04 sample exhibits the greatest contribution of the surface oxygen linked to Pr (Table 2) [39]. All of these factors may be considered responsible for the higher oxygen surface exchange rate for the PCNCO04 sample compared to the PCNCO03 one.

The effect of the diffusion retardation on the dynamics of exchange with $^{18}O_2$ can be demonstrated qualitatively by comparing the dynamic extent of exchange (X), defined as the amount of oxygen substituted at a given point in time divided by its total amount in the sample (Equation 27), during TPIE $^{18}O_2$ and $C^{18}O_2$ [41] runs (Figure 4).

$$X = \frac{1}{N}\frac{2C_{O_2}U}{\alpha_{input}R_T}\int_{T_0}^{T_{end}}(\alpha_{input} - \alpha_G)dT \qquad (27)$$

where N is the total amount of oxygen atoms in the sample, C_{O_2} is the oxygen concentration in the gas phase, U is the flow rate, R_T is the heating ramp rate.

As follows from Figure 4, the onset of isotope exchange with $^{18}O_2$ is shifted by ~ 100 °C or more towards higher temperatures compared to the exchange with $C^{18}O_2$ for all samples. Therefore, the dynamics of exchange with $^{18}O_2$ at low temperatures is limited by the exchange of oxygen in the gas phase with oxygen on the sample surface. While reaching X = 20 % (i.e. approaching the minima of the α_G curves), the extent of exchange with $C^{18}O_2$ for the PCNO and PCNCO01 samples is ~ 60 %, while for other samples, this extent is significantly lower. This suggests that the limiting effect of bulk diffusion is negligible for the PCNO and PCNCO01 samples, while it can be substantial for other samples, particularly PCNCO02.

Based on the mathematical modeling employing Model 1 (Equations 11–17) a satisfactory description of the $\alpha_G(T)$ dependencies is obtained. The oxygen tracer diffusion coefficient values are derived from the TPIE $C^{18}O_2$ data acquired in the authors' previous work [41]. The estimation errors for calculating the oxygen tracer diffusion coefficients and their effective activation energies do not exceed ± 15 % (if the other is not specified) [41]. These values (Table 3) are then used in

Table 2 – The contribution (in [%]) of the oxygen states peaks to the total O1*s* XPS spectra [39].

Sample	528.8 eV	530.15 eV	531.2 eV	0.3
	Ni–O	Pr–O	$(CO_3)^{2-}$	$(H_2O)_{ads}$
PCNO	30.1	19.5	42.0	8.4
PCNCO01	30.0	18.7	43.3	7.9
PCNCO02	27.7	16.6	45.2	10.5
PCNCO03	30.8	16.9	39.2	13.1
PCNCO04	27.5	21.3	35.5	15.6

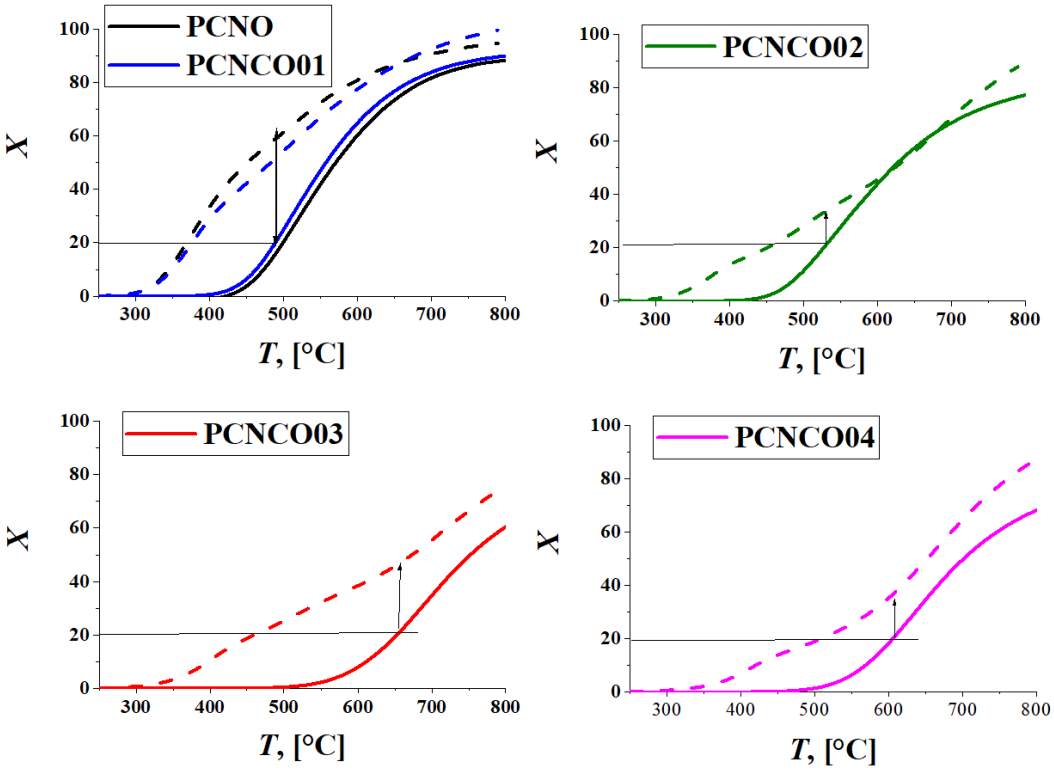

Figure 4 The dynamic extent of exchange for the $Pr_{1.6}Ca_{0.4}Ni_{1-y}Cu_yO_{4+\delta}$ samples during TPIE $^{18}O_2$ (solid lines, this work) and $C^{18}O_2$ (dashed lines, from Ref. [41]) runs.

Table 3 – The oxygen tracer diffusion coefficient (D^*) values at 700 K and their effective activation energies (E_a) for various oxygen forms (with the fraction of θ) according to the TPIE $C^{18}O_2$ data modeling [41].

Sample	O_{fast}			O_{middle}			O_{slow}		
	θ, [%]	$D^* \cdot 10^{11}$, [cm²/s]	E_a, [kJ/mol]	θ, [%]	$D^* \cdot 10^{13}$, [cm²/s]	E_a, [kJ/mol]	θ, [%]	$D^* \cdot 10^{15}$, [cm²/s]	E_a, [kJ/mol]
PCNO	77	3.6	160	23	0.6	160	0	–	–
PCNCO01	40	2.3		30	0.5	160	30	(0.1 ÷ 1)	160
PCNCO02	15	4.2		25	(0.2 ÷ 2)	160	60	1.0	160
PCNCO03	20	1.7		20	(0.1 ÷ 1)	160	60	0.7	160
PCNCO04	13	0.7		7	(0.1 ÷ 1)	160	80	1.1	160

subsequent calculations. On the other hand, the $\alpha_G(T)$ dependencies for the PCNO and PCNCO01 samples can be described using a uniform model [29] with a single diffusion coefficient within the sample bulk. This suggests no limiting effect of oxygen diffusion for the PCNO and PCNCO01 samples. For other samples, the $\alpha_G(T)$ dependencies cannot be described by a uniform model; therefore, oxygen bulk diffusion must be taken into account. The limiting effect of diffusion manifests exclusively at elevated isotope substitution extents for the PCNCO03 and PCNCO04 samples. In contrast, for the PCNCO02 sample, diffusion begins to limit the process almost immediately upon the onset of isotope exchange.

Figure 5 demonstrates the dependencies of the ^{18}O atomic (α_G) and $^{16}O^{18}O$ molecular (f_{34}) fractions in O_2 acquired for the PCNO samples. The f_{34} dependence is determined not only by the surface exchange rate, but also by the exchange mechanism. Generally, there are two types of heteroexchange R^1 (Equations 6 and 7) and R^2 (Equations 8–10) [26, 28, 29, 37, 38, 44–46]. As illustrated in Figure 5, Model 1 is incapable of explaining the f_{34} dependence, regardless of whether R^1 or R^2 is considered as the exchange mechanism. Employing the two-step model (Model 2, see Section 3.2 for details) allows a successful description of both $\alpha_G(T)$ and $f_{34}(T)$ dependencies using the R^2-type of exchange mechanism for all samples (Figure 3, upper and lower images, respectively).

The calculations demonstrated that the limiting effect of the $O_{ADS} \leftrightarrow O_S$ step occurs only for the PCNO and PCNCO01 samples. In the case of PCNCO02 sample at the onset of isotope exchange, the $O_2^{GAS} \leftrightarrow O_{ADS}$ step is limiting, then oxygen diffusion in the oxide bulk is limiting. For the PCNCO03 and PCNCO04 samples, the

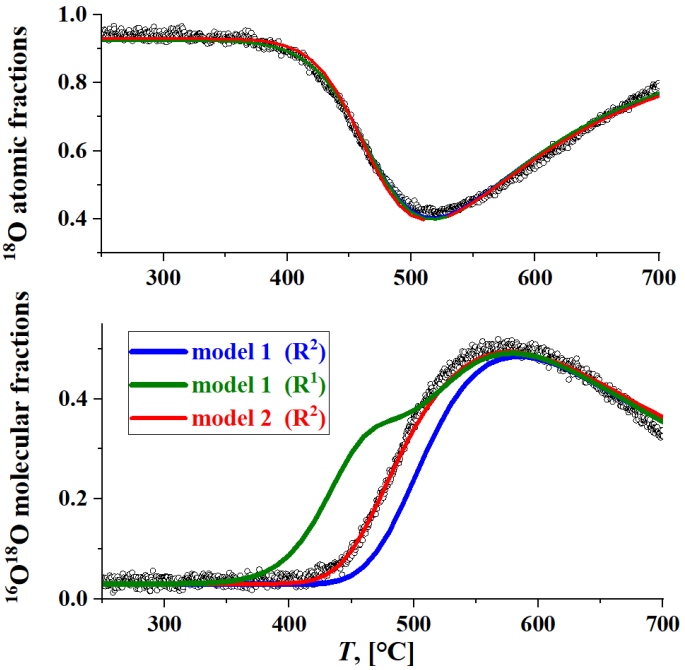

Figure 5 Temperature-programmed isotope exchange of oxygen with $^{18}O_2$ in the flow reactor for the $Pr_{1.6}Ca_{0.4}NiO_{4+\delta}$ sample. Points – experiment, lines – description using various models.

$O_2^{GAS} \leftrightarrow O_{ADS}$ step is mainly limiting, except for high oxygen isotope substitution extents. The calculated values of the surface exchange rates for the $O_2^{GAS} \leftrightarrow O_{ADS}$ (R^2) and $O_{ADS} \leftrightarrow O_S$ (K) steps are given in Table 4 and Figure 6(a). It is noteworthy that the effective activation energy values for all $Pr_{1.6}Ca_{0.4}Ni_{1-y}Cu_yO_{4+\delta}$ (y = 0.0–0.4) samples remain constant within the estimation error range, 180 kJ/mol (Table 4). The oxygen surface exchange rate is known to depend on various factors, including the frequency of exchange attempts, the surface coverage by adsorbed oxygen species, oxygen vacancies, and other oxygen forms; the enthalpies and entropies of oxygen adsorption, incorporation, and charge transfer [57–59]. The experimental findings suggest that the incorporation of Cu does not appear to exert a substantial influence on these enthalpies and entropies. However, it may have an impact on the contribution of the oxygen surface form, as evidenced by the XPS data (Table 2) [39]. Additionally, there is the possibility that the attempt frequency may be affected.

In order to compare the samples studied with the other samples and make correlations according to the ALS model, the oxygen surface exchange values (k^*) should be calculated. As follows from the calculations (Figure 6(b)), the samples possess high k^* values (~ 10^{-7}–10^{-5} cm/s at 700 °C), which is comparable or even exceeding the values for other first-order RP phases [26, 28, 29, 32, 34–36].

Table 4 – The values of the oxygen surface exchange rates (R^2, K) at 700 K and their effective activation energies ($E_a(R,K)$) according to the TPIE $^{18}O_2$ data modeling.

Sample	R^2, [μmol/(m² · s)]	K, [μmol/(m² · s)]	$E_a(R,K)$, [k]/mol]
PCNO	0.8	0.3	180(± 0.3)
PCNCO01	0.8		
PCNCO02	0.1	Not limited	
PCNCO03	0.01		
PCNCO04	0.03		

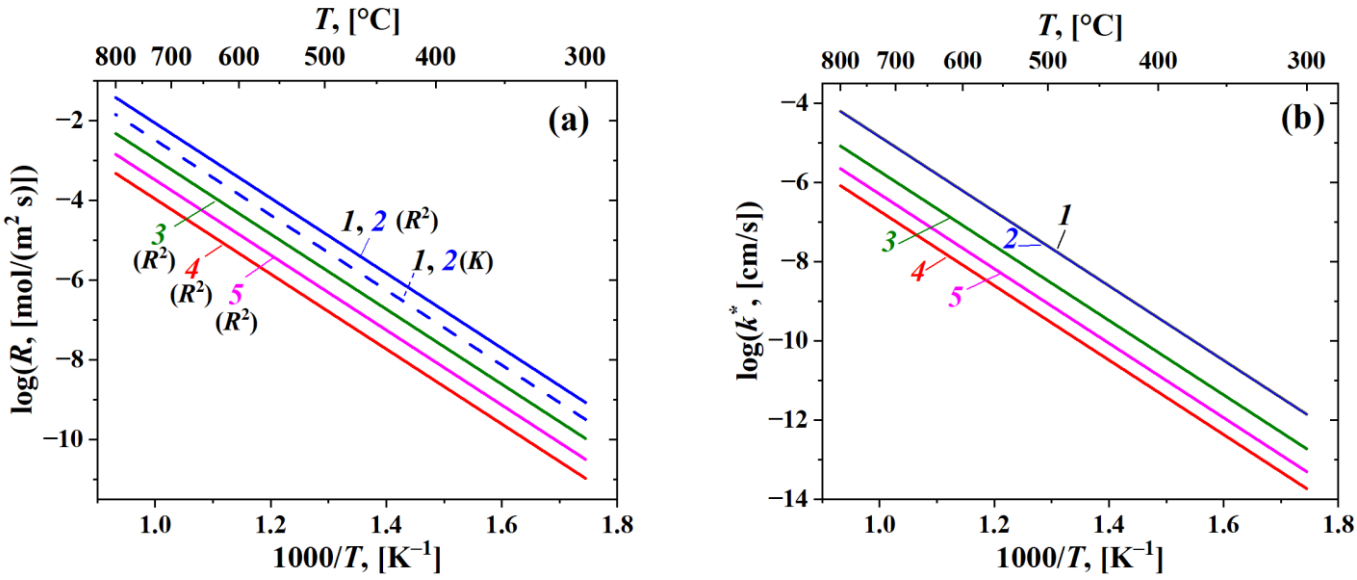

Figure 6 Arrhenius plots for oxygen surface exchange rates (a) and constants (b) according to the TPIE $^{18}O_2$ in the flow reactors for the $Pr_{1.6}Ca_{0.4}Ni_{1-y}Cu_yO_{4+\delta}$ samples, y = 0.0 (1), 0.1 (2), 0.2 (3), 0.3 (4) and 0.4 (5).

4.3. Correlation with electrochemical properties

Electrochemical impedance measurements and detailed analysis of the electrode performance were carried out in the authors' previous works [39, 40]. The polarization resistance values, R_p, for the single-layer $Pr_{1.6}Ca_{0.4}Ni_{1-y}Cu_yO_{4+\delta}$ electrodes on the SDC electrolyte were calculated as 1.88, 1.05, 1.54, 1.65 and 0.91 Ω · cm² at 700 °C for y = 0.0, 0.1, 0.2, 0.3 and 0.4, respectively. The effective activation energy values, found from the reciprocal R_p temperature dependencies, are 130, 120, 120, 120 and 90 kJ/mol for y = 0.0, 0.1, 0.2, 0.3 and 0.4 (Figure 7). The variation of the effective activation energy of R_p with the Cu content, while the effective activation energies of $D^*$and k^* are almost constant (Tables 3 and 4) may be due to the variation of the oxygen content (Equation 26) with temperature as shown by the TGA data [39, 41] as well possible deviations from the ALS model [60–62].

While analyzing the correlations of polarization resistance with oxygen content, diffusion coefficient, and surface exchange constant within the framework of the ALS model [20, 21, 28, 34, 47], the trends of decreasing R_p with increasing the $(D^*k^*)^{0.5}$ and δ values were observed (Figure 8).

The R_p and δ dependencies on the Cu content are non-monotonous, while $(D^*k^*)^{0.5}$ gradually decreases with increasing the Cu content. Especially, there are correlations of R_p with $(D^*k^*)^{0.5}$ for $Pr_{1.6}Ca_{0.4}Ni_{1-y}Cu_yO_{4+\delta}$, y = 0.1–0.3, and with δ for y = 0.1–0.4. There are deviations from direct correlations, which can be explained by the effect of microstructure and textural properties of the electrodes, and/or the variation of oxygen overstoichiometry with the temperature.

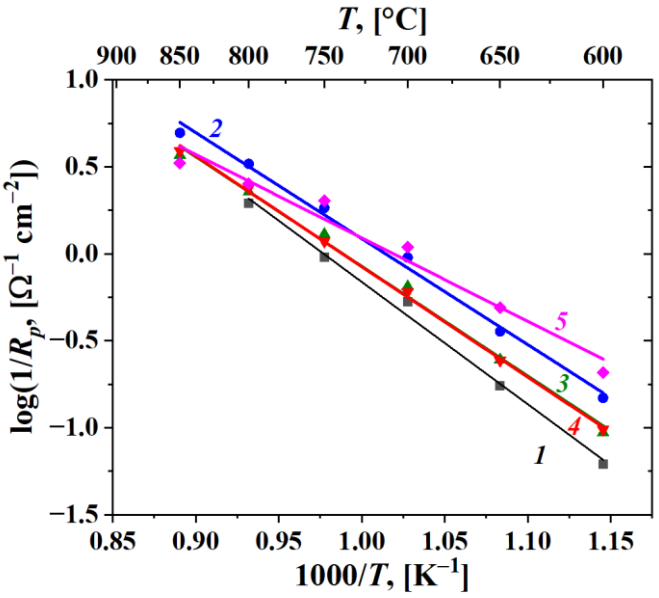

Figure 7 Arrhenius plots for the reciprocal polarization resistance of the $Pr_{1.6}Ca_{0.4}Ni_{1-y}Cu_yO_{4+\delta}$ electrodes without collector layer, y = 0.0 (1), 0.1 (2), 0.2 (3), 0.3 (4) and 0.4 (5) [39].

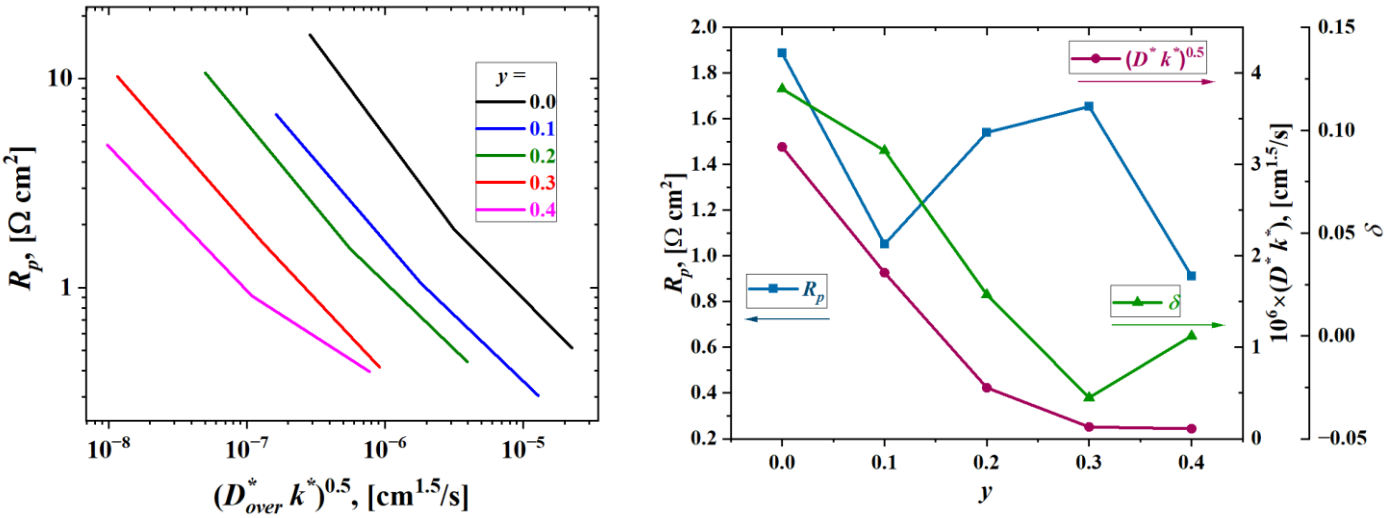

Figure 8 Correlation of polarization resistance, oxygen overstoichiometry, tracer diffusion coefficient and surface exchange constant for the $Pr_{1.6}Ca_{0.4}Ni_{1-y}Cu_yO_{4+\delta}$ series (y = 0.0–0.4).

5. Conclusions

The present study demonstrates the effect of the Cu content in the $Pr_{1.6}Ca_{0.4}Ni_{1-y}Cu_yO_{4+\delta}$ series on the oxygen surface reactivity. The temperature-programmed isotope exchange with $^{18}O_2$ studies demonstrate that the oxygen surface exchange occurs via the R^2-type of mechanism, i.e., two-atomic heteroexchange. For some samples, the limiting effect of the adsorbed oxygen incorporation into the oxide surface is shown. The oxygen surface exchange

rate tends to decrease with increasing the Cu content, which can be explained by a decrease in the highly-mobile interstitial oxygen content and mobility. The exception for the $Pr_{1.6}Ca_{0.4}Ni_{0.6}Cu_{0.4}O_{4+\delta}$ sample exhibiting higher oxygen surface exchange rate values compared to the $Pr_{1.6}Ca_{0.4}Ni_{0.7}Cu_{0.3}O_{4+\delta}$ sample can be explained by the combined effect of the sample surface properties and/or the oxygen content. Nevertheless, all samples possess high oxygen surface exchange constant values (~ 10^{-7}–10^{-5} cm/s at 700 °C) that are comparable or even exceeding the values for other first-order RP phases and is very attractive for practical application as SOFC/SOE air electrodes. The correlations of the electrode performance and materials' oxygen kinetics are demonstrated.

Supplementary materials

No supplementary materials are available.

Funding

Oxygen isotope exchange studies and mathematical modeling of the results were performed in the framework of the budget projects of the Boreskov Institute of Catalysis, Siberian Branch, Russian Academy of Sciences (projects FWUR-2024-0033 and FWUR-2024-0038, respectively). Synthesis of the materials and their characterization was done using the equipment of the Shared Access Center "Composition of compounds" in the framework of the State Assignment for the Institute of High Temperature Electrochemistry, Ural Branch, Russian Academy of Sciences (project No 125020501556-0).

Acknowledgments

The authors are grateful to Tatiana Zhulanova (IHTE UB RAS) for the synthesis of the materials, Sergey Pikalov (IMET UB RAS), Dr. Elena Filonova (UrFU) for the XRD characterizations and calculations and Yulia Fedorova (BIC SB RAS) for the measurement of true and bulk density of the samples.

Author contributions

Vladislav Sadykov: Conceptualization; Supervision; Writing – Review & Editing.

Ekaterina Sadovskaya: Data curation; Formal analysis; Methodology; Visualization; Writing – Original draft.

Nikita Eremeev: Investigation; Visualization; Writing – Original draft.

Elena Pikalova: Conceptualization; Formal analysis; Supervision; Visualization; Writing – Review & Editing.

Conflict of interest

The authors declare no conflict of interest.

Additional information

Scopus author IDs:

Vladislav Sadykov, Scopus Author ID: 7006677003, 57200684813;

Ekaterina Sadovskaya, Scopus Author ID: 57202034821, 57204295192;

Nikita Eremeev, Scopus Author ID: 55645818400;

Elena Pikalova, Scopus Author ID: 16242376500.

Websites:

Federal Research Center Boreskov Institute of Catalysis SB RAS https://en.catalysis.ru/;

Institute of High-Temperature Electrochemistry UB RAS, https://ihte.ru/.

References

1. Peng C, Han X, Mabaleha S, Kwong P, et al., Recent advances in perovskite air electrode materials for protonic solid oxide electrochemical cells, Energy Environ. Sci., **18(10)** (2025) 4555–4595. https://doi.org/10.1039/D5EE00983A

2. Liu F, Su Z, Li H, Wang Q, et al., Status and prospects of electrode materials for symmetrical solid oxide fuel cells: A concise review, Ionics, **31(5)** (2025) 3877–3894. https://doi.org/10.1007/s11581-025-06182-8

3. Chen X, Tan Y, Li Z, Liu T, et al., Advanced air electrodes for reversible protonic ceramic electrochemical cells: A comprehensive review, Adv. Mater., (2025) 2418620. https://doi.org/10.1002/adma.202418620

4. Kang HC, Park YJ, Baek SY, Kim J, et al., Recent breakthroughs in cathode of protonic ceramic fuel cells: Materials, functionalization, and future perspectives, InfoMat, (2025) e70025. https://doi.org/10.1002/inf2.70025

5. Zhu Y, Tang Z, Yuan L, Li B, et al., Beyond conventional structures: Emerging complex metal oxides for efficient oxygen and hydrogen electrocatalysis, Chem. Soc. Rev., **54(2)** (2025) 1027–1092. https://doi.org/10.1039/D3CS01020A

6. Samreen A, Ali MS, Huzaifa M, Ali N, et al., Advancements in perovskite-based cathode materials for solid oxide fuel cells: A comprehensive review, Chem. Rec., **24(1)** (2024) e202300247. https://doi.org/10.1002/tcr.202300247

7. Jiang S, Zheng X, Sun W, Toward advanced fuel electrodes for high-performance proton-conducting ceramic cells, Adv. Energy Mater., **15(4)** (2025) 2403745. https://doi.org/10.1002/aenm.202403745

8. Yatoo MA, Skinner SJ, Ruddlesden-Popper phase materials for solid oxide fuel cell cathodes: A short review, Mater. Today: Proc., **56(6)** (2022) 3747–3754. https://doi.org/10.1016/j.matpr.2021.12.537

9. Qu J, Wang X, Zhang J, Shi H, et al., Gùtǐ yǎnghuà wù ránliào diànchí Ruddlesden-Popper xíng yǎnghuà wù yángjí de yánjiū jìnzhǎn [Recent advances in Ruddlesden–Popper oxide for solid oxide fuel cells anodes], J. Funct. Mater. / Gongneng Cailiao, **55(9)** (2024) 9078–9086. Chinese. https://doi.org/10.3969/j.issn.1001-9731.2024.09.010

10. Zhu S, Fan F, Li Z, Wu J, et al., Metal exsolution from perovskite-based anodes in solid oxide fuel cells, Chem. Commun., **60(9)** (2024) 1062–1071. https://doi.org/10.1039/D3CC05688K

11. Tong J, Zhang P, Zhuang F, Zheng Y, et al., Mixed-conducting ceramic membrane reactors for hydrogen production, React. Chem. Eng., **9(12)** (2024) 3072–3099. https://doi.org/10.1039/D4RE00372A

12. Lu Q, Papaioannou EI, Development of mixed ionic and electronic conducting materials for gas separation membranes: A critical overview, Chem. Eng. J., **496** (2024) 153791. https://doi.org/10.1016/j.cej.2024.153791

13. Kwon Y-I, Nam GD, Lee G, Choi S, et al., Recent progress and challenges in mixed ionic–electronic conducting membranes for oxygen separation, Adv. Energy Sustain. Res., **3(11)** (2022) 2200086. https://doi.org/10.1002/aesr.202200086

14. Wang P, Liao L, Chu H, Xie Y, et al., Recent advances in Ruddlesden–Popper phase-layered perovskite Sr_2TiO_4 photocatalysts, Nanomaterials, **15(1)** (2025) 20. https://doi.org/10.3390/nano15010020

15. Zhou C, Guo W, Fan J, Shi N, et al., Recent advances and future perspectives of Ruddlesden–Popper perovskite oxides electrolytes for all-solid-state batteries, Infomat, **6(8)** (2024) e12563. https://doi.org/10.1002/inf2.12563

16. Neelakandan M, Dhandapani P, Ramasamy S, Duraisamy R, et al., A review on perovskite oxides and their composites as electrode materials for supercapacitors, RSC Adv., **15(21)** (2025) 16766–16791. https://doi.org/10.1039/D5RA01950H

17. Desta HG, Gebreslassie G, Zhang J, Lin B, et al., Enhancing performance of lower-temperature solid oxide fuel cell cathodes through surface engineering, Prog. Mater. Sci., **147** (2025) 101353. https://doi.org/10.1016/j.pmatsci.2024.101353

18. Yang G, Jung W, Ahn S-J, Lee D, Controlling the oxygen electrocatalysis on perovskite and layered oxide thin films for solid oxide fuel cell cathodes, Appl. Sci., **9(5)** (2019) 1030. https://doi.org/10.3390/app9051030

19. Sadykov VA, Eremeev NF, Shlyakhtina AV, Pikalova EYu, Advances in alternative metal oxide materials of various structures for electrochemical and catalytic applications, Int. J. Hydrogen Energy, **94** (2024) 179–208. https://doi.org/10.1016/j.ijhydene.2024.11.072

20. Adler SB, Factors governing oxygen reduction in solid oxide fuel cell cathodes, Chem. Rev., **104(10)** (2004) 4791–4844. https://doi.org/10.1021/cr020724o

21. Adler SB, Lane JA, Steele BCH, Electrode kinetics of porous mixed-conducting oxygen electrodes, J. Electrochem. Soc., **143(11)** (1996) 3554–3564. https://doi.org/10.1149/1.1837252

22. Yang S, Liu G, Li W, Sabolsky EM, et al., Ab initio study on the effect of *A*-site doping on the stability, equilibrium volume, activation energy barrier, and oxygen diffusivity in $La_{2-x}A_xNiO_{4+\delta}$, Int. J. Hydrogen Energy, **119** (2025) 235–251. https://doi.org/10.1016/j.ijhydene.2025.03.239

23. Li X, Benedek NA, Enhancement of ionic transport in complex oxides through soft lattice modes and epitaxial strain, Chem. Mater., **27(7)** (2015) 2647–2652. https://doi.org/10.1021/acs.chemmater.5b00445

24. Lee D, Lee HN, Controlling oxygen mobility in Ruddlesden–Popper oxides, Materials, **10(4)** (2017) 368. https://doi.org/10.3390/ma10040368

25. Sadykov V, Pikalova E, Eremeev N, Shubin A, et al., Oxygen transport in Pr nickelates: Elucidation of atomic-scale features, Solid State Ionics, **344** (2020) 115155. https://doi.org/10.1016/j.ssi.2019.115155

26. Ananyev MV, Tropin ES, Eremin VA, Farlenkov AS, et al., Oxygen isotope exchange in $La_2NiO_{4\pm\delta}$, Phys. Chem. Chem. Phys., **18(13)** (2016) 9102–9111. https://doi.org/10.1039/C5CP05984D

27. Grobovoy IS, Kolchugin AA, Pikalova EYu, Suntsov AYu, Defect formation and thermodynamic properties of Ca-doped La_2NiO_4 oxides, Inorg. Chem. Commun., **179(2)** (2025) 114823. https://doi.org/10.1016/j.inoche.2025.114823

28. Pikalova EYu, Guseva EM, Filonova EA, Short review on recent studies and prospects of application of rare-earth-doped $La_2NiO_{4+\delta}$ as air electrodes for solid oxide electrochemical cells, Electrochem. Mater. Technol., **2(4)** (2024) 20232025. https://doi.org/10.15826/elmattech.2023.2.025

29. Sadykov V, Pikalova E, Sadovskaya E, Shlyakhtina A, et al., Design of mixed ionic-electronic materials for permselective membranes and solid oxide fuel cells based on their oxygen and hydrogen mobility, Membranes, **13(8)** (2023) 698. https://doi.org/10.3390/membranes13080698

30. Amov G, Skinner SJ, Recent developments in Ruddlesden–Popper nickelate systems for solid oxide fuel cell cathodes, J. Solid State Electrochem., **10(8)** (2006) 538–546. https://doi.org/10.1007/s10008-006-0127-x

31. Yin B, Li Y, Sun N, Ji X, et al., Activating ORR and OER in Ruddlesden-Popper based catalysts by enhancing interstitial oxygen and lattice oxygen redox reactions, Electrochim. Acta, **370** (2021) 137747. https://doi.org/10.1016/j.electacta.2021.137747

32. Li W, Guan B, Zhang X, Yan J, et al., New mechanistic insight into the oxygen reduction reaction on Ruddlesden–Popper cathodes for intermediate-temperature solid oxide fuel cells, Phys. Chem. Chem. Phys., **18(12)** (2016) 8502–8511. https://doi.org/10.1039/C6CP00056H

33. Gu X-K, Nikolla E, Design of Ruddlesden–Popper oxides with optimal surface oxygen exchange properties for oxygen reduction and evolution, ACS Catal., **7(9)** (2017) 5912–5920. https://doi.org/10.1021/acscatal.7b01483

34. Pikalova EYu, Sadykov VA, Filonova EA, Eremeev NF, et al., Structure, oxygen transport properties and electrode performance of Ca-substituted Nd_2NiO_4, Solid State Ionics, **335** (2019) 53–60. https://doi.org/10.1016/j.ssi.2019.02.012

35. Kolchugin AA, Pikalova EYu, Bogdanovich NM, Bronin DI, et al., Structural, electrical and electrochemical properties of calcium-doped lanthanum nickelate, Solid State Ionics, **288** (2016) 48–53. https://doi.org/10.1016/j.ssi.2016.01.035

36. Tropin E, Ananyev M, Porotnikova N, Khodimchuk A, et al., Oxygen surface exchange and diffusion in $Pr_{1.75}Sr_{0.25}Ni_{0.75}Co_{0.25}O_{4\pm\delta}$, Phys. Chem. Chem. Phys., **21(9)** (2019) 4779–4790. https://doi.org/10.1039/C9CP00172G

37. Muzykantov VS, Popovski VV, Boreskov GK, Kinetika izotopnogo obmena v sisteme molekulyarnyi kislorod – tvyodyi okisel [Kinetics of isotope exchange in molecular oxygen – solid oxide system], Kinet. Katal., **5(4)** (1964) 624–629. Russian.

38. Muzykantov VS, Popovski VV, Boreskov GK, Kinetika i mekhanizm izotopnogo obmena v sisteme molekulyarnyi kislorod – tvyodyi okisel [Kinetics and mechanism of isotope exchange in molecular oxygen – solid oxide system]. In: Problemy kinetiki i kataliza, T.12 [Problems in kinetics and catalysis, V.12]. Moscow: Nauka, 1968. pp. 155–159. Russian.

39. Pikalova E, Zhulanova T, Ivanova A, Tarutin A, et al., Optimized $Pr_{1.6}Ca_{0.4}Ni_{1-y}Cu_yO_{4+\delta}$ phases as promising electrode materials for CeO_2- and $BaCe(Zr)O_3$-based electrochemical cells, Ceram. Int., **50(20C)** (2024) 40476–40491. https://doi.org/10.1016/j.ceramint.2024.06.048

40. Zhulanova T, Filonova E, Ivanova A, Russkikh O, et al., Control physicochemical and electrochemical properties of $Pr_{1.6}Ca_{0.4}Ni_{0.6}Cu_{0.4}O_{4+\delta}$ as a prospective cathode material for solid oxide cells through the synthesis process, Solid State Sci., **156** (2024) 107671. https://doi.org/10.1016/j.solidstatesciences.2024.107671

41. Sadykov V, Eremeev N, Sadovskaya E, Zhulanova T, et al., Impact of calcium and copper co-doping on the oxygen transport of layered nickelates: A case study of $Pr_{1.6}Ca_{0.4}Ni_{1-y}Cu_yO_{4+\delta}$ and a comparative analysis, Chim. Tech. Acta, **11(4)** (2024) 20241141l. https://doi.org/10.15826/chimtech.2024.11.4.11

42. Sadykov VA, Sadovskaya EM, Uvarov NF, Methods of isotopic relaxations for estimation of oxygen diffusion coefficients in solid electrolytes and materials with mixed ionic-electronic conductivity, Russ. J. Electrochem., **51(5)** (2015) 458–467. https://doi.org/10.1134/S1023193515050109

43. Sadykov V, Sadovskaya E, Bobin A, Kharlamova T, et al., Temperature-Programmed $C^{18}O_2$ SSITKA for powders of fast oxide-ion conductors: Estimation of oxygen self-diffusion coefficients, Solid State Ionics, **271** (2015) 69–72. https://doi.org/10.1016/j.ssi.2014.11.004

44. Boreskov GK, Muzykantov VS, Investigation of oxide-type oxidation catalysts by reactions of oxygen isotopic exchange, Ann. N. Y. Acad. Sci., **213(1)** (1973) 137–170. https://doi.org/10.1111/j.1749-6632.1973.tb51065.x

45. Muzykantov VS, Isotopic studies of dioxygen activation on oxide catalysts for oxidation: Problems, results and perspectives, React. Kinet. Catal. Lett., **35(1–2)** (1987) 437–447. https://doi.org/10.1007/BF02062178

46. den Otter MW, Boukamp BA, Bouwmeester HJM, Theory of oxygen isotope exchange, Solid State Ionics, **139(1–2)** (2001) 89–94. https://doi.org/10.1016/S0167-2738(00)00801-8

47. Huang Q-A, Hui R, Wang B, Zhang J, A review of AC impedance modeling and validation in SOFC diagnosis, Electrochim. Acta, **52(28)** (2007) 8144–64. https://doi.org/10.1016/j.electacta.2007.05.071

48. Ananyev MV, Kurumchin EKh, Porotnikova NM, Effect of oxygen nonstoichiometry on kinetics of oxygen exchange and diffusion in lanthanum-strontium cobaltites, Russ. J. Electrochem., **46(7)** (2010) 789–797. https://doi.org/10.1134/S1023193510070128

49. Aguadero A, Alonso J, Escudero M, Daza L, Evaluation of the $La_2Ni_{1-x}Cu_xO_{4+\delta}$ system as SOFC cathode material with 8YSZ and LSGM as electrolytes, Solid State Ionics, **179(11–12)** (2008) 393–400. https://doi.org/10.1016/j.ssi.2008.01.099

50. Sakai M, Wang C, Okiba T, Soga H, et al., Thermal analysis of structural phase transition behavior of $Ln_2Ni_{1-x}Cu_xO_{4+\delta}$ (Ln = Nd, Pr) under various oxygen partial pressures, J. Therm. Anal. Calorim., **135(5)** (2019) 2765–2774. https://doi.org/10.1007/s10973-018-7621-0

51. Popovski VV, Boreskov GK, Kinetika izotopnogo obmena molekulyarnogo kisloroda s kislorodom poverkhnosti okislov zheleza, kobal'ta, nikelya i medi [Kinetics of isotope exchange of molecular O_2 with oxide surfaces of Fe, Co, Ni, and Cu], Kinet. Catal., **1(4)** (1960) 566–575. Russian.

52. Kaluzhskikh MS, Kazakov SM, Mazo GN, Istomin SYa, et al., High-temperature crystal structure and transport properties of the layered cuprates Ln_2CuO_4, Ln = Pr, Nd and Sm, J. Solid State Chem., **184(3)** (2011) 698–704. https://doi.org/10.1016/j.jssc.2011.01.035

53. Miyoshi S, Furuno T, Sangoanruang O, Matsumoto H, et al., Mixed conductivity and oxygen permeability of doped Pr_2NiO_4-based oxides, J. Electrochem. Soc., **154(1)** (2007) B57–B62. https://doi.org/10.1149/1.2387103

54. Yashima M, Yamada H, Nuansaeng S, Ishihara T, Role of Ga^{3+} and Cu^{2+} in the high interstitial oxide-ion diffusivity of Pr_2NiO_4-based oxides: design concept of interstitial ion conductors through the higher-valence d^{10} dopant and Jahn-Teller effect, Chem. Mater., **24(21)** (2012) 4100–4113. https://doi.org/10.1021/cm3021287

55. Biesinger MC, Payne BP, Lau LWM, Gerson A, et al., X-ray photoelectron spectroscopic chemical state quantification of mixed nickel metal, oxide and hydroxide systems, Surf. Interface Anal., **41(4)** (2009) 324–332. https://doi.org/10.1002/sia.3026

56. Vincent Crist B. Handbooks of Monochromatic XPS Spectra: Volume 2: Commercially Pure Binary Oxides and a few Common Carbonates and Hydroxides: John Wiley & Sons; 2000. 27 p.

57. Ishihara T. Perovskite oxide for solid oxide fuel cells. New York: Springer Science + Business Media, LLC; 2009. 302 p.

58. Kilner JA, De Souza RA, Fullarton IC, Surface exchange of oxygen in mixed conducting perovskite oxides, Solid State Ionics, **86–88(2)** (1996) 703–709. https://doi.org/10.1016/0167-2738(96)00153-1

59. De Souza RA, Limits to the rate of oxygen transport in mixed-conducting oxides, J. Mater. Chem. A, **5(38)** (2017) 20334–20350. https://doi.org/10.1039/C7TA04266C

60. Abd Aziz AJ, Baharuddin NA, Lim BH, Characterization of oxygen diffusion and catalytic behavior of composite materials in solid oxide fuel cells using the non-destructive Adler-Lane-Steele method, e-J, Nondestructi. Testing, **29(6)** (2024). https://doi.org/10.58286/30310

61. Endler-Schuck C, Joos J, Niedrig C, Weber A, et al., The chemical oxygen surface exchange and bulk diffusion coefficient determined by impedance spectroscopy of porous $La_{0.58}Sr_{0.4}Co_{0.2}Fe_{0.8}O_{3-\delta}$ (LSCF) cathodes, Solid State Ionics, **269** (2015) 67–79. https://doi.org/10.1016/j.ssi.2014.11.018

62. Goel V, Cox D, Barnett SA, Thornto K, Simulation of the electrochemical impedance in a three-dimensional, complex microstructure of solid oxide fuel cell cathode and its application in the microstructure characterization, Front. Chem., **9** (2021) 627699. https://doi.org/10.3389/fchem.2021.627699